

Numerical simulation of bubble deformation and breakup under simple linear shear flows

Mitsuhiro Ohta^{a,b,*}, Tetsuya Ueta^b, Yozo Toei^c, Edwin Jimenez^d, Mark Sussman^e

^a*Department of Mechanical Science, Graduate School of Technology, Industrial and Social Sciences, Tokushima University, 2-1 Minamijyousanjima-cho, Tokushima 770-8506, Japan*

^b*Department of Mechanical Engineering, Graduate School of Technology, Industrial and Social Sciences, Tokushima University, 2-1 Minamijyousanjima-cho, Tokushima 770-8506, Japan*

^c*High Performance Plastics Company, Sekisui Chemical Co., Ltd., 2-1 Hyakuyama, Mishimagun Shimamoto-cho, Osaka 618-0021, Japan*

^d*Spectral Numerical, LLC, 1942 Broadway St., STE 314C, Boulder, CO 80302, USA*

^e*Department of Mathematics, Florida State University, Tallahassee, FL 32306, USA*

Abstract

Numerical simulations are presented for the deformation and breakup of a bubble in liquids undergoing simple linear shear flow. Numerical results are obtained using a projection method for incompressible two-phase flow in which the method represents interfaces using the sharp interface coupled level set and volume of fluid (CLSOVF) method. To verify our numerical algorithm and provide a basis for comparison, we also present simulation results that compare with previous, more popular, drop deformation and rupture simulations. The numerical results reveal that the shear-induced bubble deformation and breakup process differs significantly from that of the analogous drop system under similar flow conditions. The first distinguishing factor for bubble breakup is that the magnitude of shear flow necessary for causing rupture is much larger than that in the drop system case. In other words, a larger Reynolds number is needed to induce bubble breakup. The second distinct feature of the bubble system versus the drop system is that the bubble does not maintain a stable deformed shape as the system parameters approach the critical “breakup” Reynolds number. It is asserted that the differences in morphology for a bubble undergoing breakup versus a drop in the same process can be attributed to the density and viscosity ratio of the corresponding two-phase flow systems. The critical conditions for bubble breakup with respect to the Reynolds and capillary numbers are determined for several cases.

Keywords: Bubble deformation, bubble breakup, shear flow, CFD

*Corresponding author: m-ohta@tokushima-u.ac.jp

1 **1. Introduction**

2 Bubble dynamics in shear flow, including breakup, is critically important
3 for various gas-liquid scientific and engineering processes. We refer the reader
4 to the following experimental studies relating to bubble deformation in foaming
5 processes, microfluidic devices, microbubbles in the blood circulation system,
6 materials processing, pharmaceuticals, minerals engineering, bubble column re-
7 actor, and cosmetics[4, 25, 3, 8, 9, 50, 10, 53]. In particular, it is the study of
8 bubble deformation as it pertains to high-performance plastics applications that
9 motivate this work. This article presents computational studies of shear-driven
10 deformation and breakup of a bubble in insoluble viscous liquids. Studying
11 bubble break-up, vis a vis that of the drop, via computation rather than (ter-
12 restrial) experiments simplifies the process of setting a combination of precise,
13 simple shear flow conditions, low Ca ($Ca = \mu_m U / \sigma$) conditions, low-density
14 ratio, and low viscosity ratios. The physical properties that distinguish bubble
15 and drop studies are expressed in terms of the density ratio $\lambda = \rho_b / \rho_m$ and the
16 viscosity ratio $\eta = \mu_b / \mu_m$, where ρ is the fluid density, μ is the viscosity and the
17 subscripts “b” and “m” denote the “bubble” or “drop” and the “matrix fluid”,
18 respectively. For a bubble in an insoluble, viscous liquid, $\lambda \simeq 0$ and $\eta \simeq 0$,
19 whereas most (terrestrial) studies dealing with a drop in an immiscible viscous
20 liquid take $\lambda = 1$ and $\eta \simeq 1$. In this work, we focus on identifying critical flow
21 states numerically, in terms of dimensionless quantities, that specify the extreme
22 conditions at which a bubble in shear flow first transitions from deformation to
23 breakup. We validate our numerical method by examining the sensitivity of the
24 critical bubble deformation and break-up flow states with respect to the grid
25 size. An advantage of studying shear-driven bubble deformation and breakup
26 computationally rather than experimentally is that we can easily modify fluid
27 physical properties and external properties (e.g. the gravity force, in order to
28 compare with the analogous drop case) in order to isolate the sensitivity of
29 deformation and breakup to physical parameters. In our computations, the
30 time-evolution of the boundary between gas and liquid is tracked with a cou-
31 pled level set/volume-of-fluid (CLSVOF) interface capturing algorithm [42, 44].
32 The rationale for the CLSVOF method is that the hybrid method represents
33 the (complex) gas-liquid interfaces with minimal volume loss (property of the
34 volume-of-fluid method) and minimal error in the approximation of the surface
35 tension force (property of the level set method). We focus on determining crit-
36 ical physical conditions in which the breakup of a bubble occurs in shear flow
37 because it is important to identify the parameter regimes in which a relatively
38 simple system transitions from stable to unstable. Specifically, we ascertain
39 the critical Reynolds number (Re_c) corresponding to the bubble breakup onset
40 condition as a function of Ca . In previous studies on the motion of bubble de-
41 formation in a simple shear flow [37, 25], only findings for bubble deformation
42 under very low Re number conditions ($Re \ll 1$) have been reported. This is
43 understandable since a low Reynolds number matrix fluid mitigates the effect
44 of gravity on distorting the comparison with the drop case. In this work, we de-
45 termine, for the first time, the critical Reynolds number ($Re \gg 1$) that leads to

46 bubble breakup. Additionally, our computational studies reveal characteristics
47 that distinguish a drop’s deformation and breakup processes versus those of a
48 bubble. We remark that there have been a number of articles on the study of
49 lift of slightly deformable bubbles[11, 23]. We reiterate, though, that for bubble
50 deformation and breakup in shear flows, only a few articles exist: [52, 51, 38].
51 These previous studies mainly examined the dynamics (e.g., rotation angle) of
52 bubble deformation in shear flow. Concerning bubble breakup, Wei et al. [52]
53 presented one numerical result for a bubble breakup process under the condition
54 of Ca (capillary number) = 35. Sharifi et al[38] presented two results for bubble
55 breakup corresponding to $Ca = 7.5$ and $Ca = 11.2$. We point out that all of the
56 previous computational research on bubble deformation (and breakup) under
57 shear driven flow[52, 51, 38] use the (explicit) Lattice Boltzmann method. For
58 accurately computing the tensile strength of a bubble, and accurately computing
59 threshold parameters for break-up (what we do in this article, and what
60 was not done in previous work), it is critical that a numerical method directly
61 enforces the velocity continuity condition and the gas-liquid interface normal
62 jump conditions. We contend that a projection method (e.g. this paper and
63 [55, 56, 29]) is the more appropriate (albeit slower) method for our study rather
64 than the Lattice Boltzmann method. Also, in contrast to the Lattice Boltz-
65 mann method, our interface “capturing” method, the CLSVOF method[42, 44],
66 maintains the gas/liquid interface as sharp, enables accurate approximation of
67 the surface tension force, and by construction the CLSVOF method preserves
68 mass and volume within a fraction of a percent. The results that we present in
69 this article (see e.g. section 3.3.2) regarding measuring the tensile strength of
70 a bubble are unique and validated with respect to comparisons with previous
71 experimental data and grid refinement studies. Admittadly, each simulation on
72 the finest resolution takes over a half a year to complete on a workstation be-
73 cause of the following unavoidable factors: (i) the large density-ratio projection
74 method requires the solution of a large sparse, ill-conditioned, matrix system at
75 each time step, (ii) the finer the mesh, the more precise the measured threshold,
76 and right at the threshold (Taylor Deformation parameter $D \approx 1$), oscillatory
77 behaviour is observed delaying the determination of breakup or not. Finally,
78 the larger the deformation parameter D , the longer we must make our compu-
79 tational domain (bigger domain aspect ratio!) thereby adversely effecting the
80 condition number even more for carrying our the pressure projection.

81 To highlight the mechanisms of bubble deformation and breakup in a shear
82 flow, we juxtapose the bubble results with those of a drop (for terrestrial ex-
83 periments, when the density ratio of drop to matrix is very close to one!). We
84 remark that while the study of critical tensile strength parameters for the bub-
85 ble is sparse, there have been many studies for the simpler drop problem. For
86 completeness, we give a brief overview of previous “tensile strength” studies
87 pertaining to drops. The study of the deformation and breakup of a drop in
88 immiscible viscous liquids undergoing simple linear shear flow has been inves-
89 tigated extensively due to its fundamental importance to emulsion processes,
90 materials processing, mixing, and reaction devices. The pioneering experimen-
91 tal work on this problem was performed by Taylor in the early 1930s [47, 48],

92 and the subsequent theoretical and experimental progress up to the 1980s and
93 1990s was reviewed in [30] and [39], respectively. By the 2000s, progress in com-
94 putational fluid dynamics (CFD) techniques and increased access to powerful
95 computing resources led to a surge of research focused on direct simulations
96 of this problem. In particular, detailed computational investigations of drop
97 breakup, based on a Volume-of-Fluid (VOF) method [13] were presented in
98 [24, 34, 36, 35, 20, 31, 32, 33]. Since then, the literature on computational stud-
99 ies on the deformation and breakup of a single or several drops in shear flow
100 has continued to grow [6, 15, 54, 2, 17, 7, 21, 22, 16, 12, 1, 57] and a variety
101 of numerical techniques have been developed to tackle this problem, including
102 boundary-integral approaches [5, 18], lattice Boltzmann methods [14, 21], front
103 tracking schemes [49], and interface-capturing level set methods [43]. Thus, a
104 lot of studies about the deformation and breakup of a drop in simple linear shear
105 have been presented so far. In contrast, few studies have been conducted on
106 bubble deformation and breakup. We reiterate why there have been few studies
107 regarding the “tensile strength” of bubbles. Experimentally, in the moderate
108 to high Reynolds number regime, and low Capillary number regime, one is re-
109 stricted to microgravity conditions. Computational experiments are difficult
110 too. In order to accurately compute the tensile strength of a bubble, one must
111 resort to a combination of parallel computing, the multigrid preconditioned
112 conjugate gradient method[46, 44] for poorly conditioned large sparse matrix
113 systems, adaptive mesh refinement[58, 44], and a robust, volume preserving
114 interface tracking method (we use the CLSVOF method[42, 44]).

115 **2. Problem Description**

116 Figure 1(a) shows a schematic of the computational system for our studies
117 of a bubble (or drop) in shear flow. The computational domain consists of a
118 three-dimensional rectangular domain of L (length) $\times W$ (width) $\times H$ (height).
119 The size of L , W and H was determined after consideration of numerical result
120 sensitivity to domain size; numerical studies of domain-size dependence are
121 presented in Section 3.3. All computational results that follow were obtained
122 from numerical solutions of the three-dimensional governing equations for gas-
123 liquid/liquid-liquid flows. Computations are initialized with a spherical bubble
124 (or drop) of radius $R = 5$ mm set at the center of the computational domain.
125 The bubble (or drop) is then subjected to a linear shear flow generated by the
126 motion of the top and bottom plates, which have constant velocity $+V$ and
127 $-V$, respectively. In the interior of the domain, the initial velocity condition
128 is assumed to be a simple linear profile and periodic boundary conditions are
129 imposed along the x and y directions. Mathematically, the initial and boundary

130 conditions are described as follows:

$$\begin{aligned}\phi(x, y, z, 0) &= \sqrt{(x - \frac{L}{2})^2 + (y - \frac{W}{2})^2 + (z - \frac{H}{2})^2 - R} \quad (1) \\ \mathbf{u}(x, y, z, 0) &= \begin{pmatrix} \frac{2V}{H}(z - \frac{H}{2}) \\ 0 \\ 0 \end{pmatrix} \\ \phi(x + L, y, z, t) &= \phi(x, y, z, t) \quad \phi(x, y + W, z, t) = \phi(x, y, z, t) \\ \mathbf{u}(x, y, H, t) &= \begin{pmatrix} V \\ 0 \\ 0 \end{pmatrix} \quad \mathbf{u}(x, y, 0, t) = \begin{pmatrix} -V \\ 0 \\ 0 \end{pmatrix} \\ \mathbf{u}(x + L, y, z, t) &= \mathbf{u}(x, y, z, t) \quad \mathbf{u}(x, y + W, z, t) = \mathbf{u}(x, y, z, t)\end{aligned}$$

131 $\phi(x, y, z, t)$ is a material indicator function which is positive in the “matrix”
132 fluid and negative in the bubble (or drop) fluid. $\mathbf{u}(x, y, z, t)$ is the velocity.

133 Common dimensionless physical parameters used to describe gas-liquid or
134 liquid-liquid two-phase flows include the Reynolds (Re), Weber (We) (or Ca (=
135 We/Re)) and Froude (Fr) numbers. Gas-Liquid and Liquid-Liquid two-phase
136 flow problems are also determined by the density ratio λ and the viscosity ratio
137 η . In the present study, in order to clearly isolate only the effects of λ and η ,
138 the effect of gravity is not considered ($g = 0$) so that we ignore the effect of the
139 Fr number $\left(= \frac{\Gamma R}{\sqrt{gR}}\right)$.

140 When comparing with previous drop studies, we fix $\lambda = 1$ for the drop cases.
141 As a result, (for $\lambda = 1$) the following dimensionless physical parameters are used
142 to describe the problem of drop deformation/breakup in shear flow

$$Re = \frac{\rho_m U R}{\mu_m}, \quad Ca = \frac{\mu_m U}{\sigma}, \quad \eta = \frac{\mu_b}{\mu_m} \quad m = \text{matrix fluid} \quad (2)$$

143 U is the velocity scale and σ denotes the surface tension. For the problem of
144 shear-induced drop deformation and breakup, the velocity is set to $U = \Gamma R$,
145 where the shear-rate is $\Gamma = 2V/H$. As mentioned in the introduction, most
146 previous drop studies set $\eta = 1$ (e.g. Li et al. [24]). Thus, for comparison
147 with previous drop deformation and breakup problems, we set $\lambda = \eta = 1$ (and
148 also neglect the effect of gravity so that $g = 0$). On the other hand, in our
149 computations for bubble deformation, we set the density and viscosity of air to
150 be $\rho_b = 1.2 \text{ kg/m}^3$ and $\mu_b = 1.8 \times 10^{-5} \text{ Pa}\cdot\text{s}$ respectively. We emphasize that for
151 consistency with previous studies (Li et al. [24], Rust and Manga [37], Müller-
152 Fischer et al. [25], Komrakova et al. [21], Amani et al. [1]), we computationally
153 examine the deformation and breakup of a bubble in simple linear shear flow
154 as a function of the Re and Ca numbers. That is to say, by setting $g = 0$,
155 we are isolating the effect of only varying Re and Ca on bubble deformation
156 and breakup. In our controlled study, we determine the critical Re_c versus Ca
157 curve in which Re_c corresponds to the threshold of bubble (or drop) breakup.
158 We determine the critical Re_c versus Ca curve for strategic pairs of the density
159 ratio and viscosity ratio.

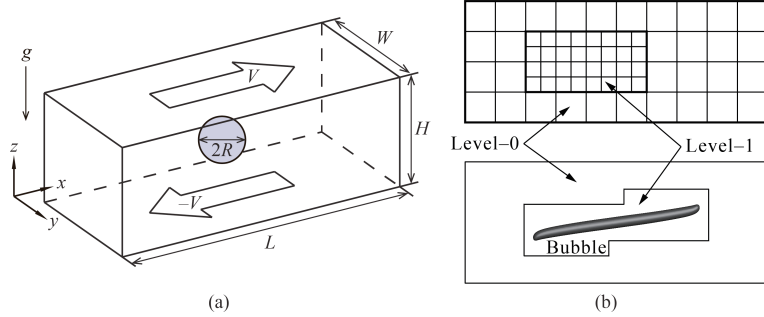


Figure 1: (a) Computational domain schematic for a bubble or drop in shear flow. Gravity is set to zero in our computations in order to isolate the effects of density and viscosity ratios. (b) (upper panel) a two-level adaptive mesh refinement (AMR) grid schematic corresponding to one of our simulations; (lower panel) snapshot of bubble deformation in simple linear shear flow.

160 In our computations, the density of the matrix fluid is fixed at $\rho_m = 1000$
 161 kg/m^3 . The surface tension at the bubble (drop) interface is $\sigma = 2.5 \times 10^{-2}$
 162 N/m . The values of Re and Ca in our simulations are controlled by changing
 163 the values of μ_m and V . Specifically, we set $\mu_m = 2.0 \times 10^{-2} \sim 6.0 \times 10^{-2}$
 164 $\text{Pa}\cdot\text{s}$ and $V = \text{about } 1.1 \sim 1.3 \text{ m/s}$. As a consequence, for studying bubble
 165 deformation and break-up, the density and viscosity ratios satisfy $\lambda = 1.2 \times 10^{-3}$
 166 and $\eta < 1.0 \times 10^{-3}$.

167 For readers' reference, we describe the effect of gravity here. When we apply
 168 $g = 9.8 \text{ m/s}^2$, Fr can be $Fr = 1.7 \sim 1.9$ in our computations. Although the
 169 values of Fr are not so large, the effect of gravity (bubble rise motion) may not
 170 be completely negligible in terms of Fr . However, bubbles in our computations
 171 reach the breakup by way of deformation very quickly at $t = \text{about } 0.5 \text{ s}$.
 172 Accordingly, it is expected that the effect of gravity (bubble rise motion) can
 173 be small for the behavior of bubble deformation and breakup around critical Re
 174 number conditions in our study.

175 3. Numerical Analysis

176 3.1. Numerical method and governing equations

177 Numerical results were obtained using the interface capturing Coupled Level
 178 Set and Volume of Fluid (CLSVOF) method (Sussman and Puckett [42], Suss-
 179 man et al. [44]), which is based on a fixed grid finite volume algorithm. The
 180 CLSVOF method is a robust numerical technique that combines some of the ad-
 181 vantages of the Volume of Fluid (VOF) method (Hirt and Nichols [13]) and the
 182 Level Set (LS) (Sussman et al. [43]) method while overcoming their weaknesses.
 183 In the VOF method, the Volume Fraction function, F , is used to represent
 184 the interface. The values of F correspond to the volume fraction of liquid in
 185 a given computational cell. In other words, $F = 0$ when a computational cell
 186 contains only gas and $F = 1$ when a computational cell contains only liquid.

187 If $0 < F < 1$, then a computational cell contains the gas-liquid interface. The
 188 VOF method has a great advantage over the LS method in that accurate algo-
 189 rithms for advecting F can be applied so that mass/volume is conserved up to
 190 machine precision while still maintaining a sharp representation of the interface.
 191 On the other hand, the disadvantage of the VOF method in comparison to the
 192 LS method is that tangled and difficult reconstruction procedures are required
 193 for determining the slope of the piecewise linear VOF reconstructed interface.
 194 In the LS method, the signed distance function ϕ (LS function) is used to track
 195 the interface. The interface is implicitly represented by the set of points in which
 196 $\phi = 0$. Liquid and gas regions are defined as $\phi > 0$ in the liquid and $\phi < 0$ in the
 197 gas, respectively. One of the advantages of the LS method is that one can track
 198 and represent smoothly the interface, but the LS method has the disadvantage
 199 that mass/volume is not explicitly conserved. In the CLSVOF method, the cou-
 200 pling between the LS function and the VOF function occurs when computing
 201 the normal of the reconstructed interface in the VOF calculation process and
 202 also when assigning the LS function with the exact signed normal distance to
 203 the reconstructed interface in the LS calculation process. That is to say, the
 204 piecewise linear approximation (the volume-of-fluid reconstruction step) for the
 205 VOF method is determined using the unit normal vector (\mathbf{n}) estimated from
 206 information of the LS function. By taking advantage of both methods, the evo-
 207 lution of the liquid-gas interface location can be computationally captured in
 208 such a way so that volume/mass is preserved to machine precision and at the
 209 same time, the interface normals and the surface tension force (which is pro-
 210 portional to the interface curvature) can be straightforwardly derived from the
 211 smooth level set function.

212 In our studies, the two-phase fluid flow is comprised of air and a viscous
 213 Newtonian liquid. The Heaviside function, $\mathcal{H}(\phi)$, which is defined as

$$\mathcal{H}(\phi) = \begin{cases} 1 & \phi \geq 0 \\ 0 & \phi < 0 \end{cases} \quad (3)$$

214 will be used below to distinguish each of the two fluids. A single set of three-
 215 dimensional equations governs the motion of both fluids, which are taken to be
 216 incompressible, and consists of the continuity equation and the Navier-Stokes
 217 equations with surface tension forces:

$$\nabla \cdot \mathbf{u} = 0 \quad (4)$$

$$\frac{\partial \mathbf{u}}{\partial t} + (\mathbf{u} \cdot \nabla) \mathbf{u} = \frac{1}{\rho} \nabla \cdot (-p \mathbf{I} + 2\mu \mathbf{D}) + \mathbf{g} - \frac{\sigma \kappa}{\rho} \nabla \mathcal{H} \quad (5)$$

218 where \mathbf{u} is the velocity vector, t represents time, p is the pressure, \mathbf{I} is the unit
 219 tensor, \mathbf{D} is the rate of deformation tensor ($\mathbf{D} = \frac{1}{2}(\nabla \mathbf{u} + (\nabla \mathbf{u})^T)$), ρ is the
 220 density, μ is the viscosity, κ is the interfacial curvature, and the Heaviside func-
 221 tion $\mathcal{H}(\phi)$ is a function of the level set (LS) function ϕ . The singular Heaviside
 222 gradient term in the right hand side of equation (5) is a body force representing
 223 the surface tension force and is equivalent to specifying that the jump in the

224 normal stress is equal to $\sigma\kappa$ (Tanguy et al. [45]). The surface tension force
 225 expressed by the singular Heaviside gradient term acts only on the gas-liquid
 226 interface. The sharp interface “Ghost Fluid Method” (Kang et al. [19]) is used
 227 to discretize the gradient of the Heaviside function as it appears in the surface
 228 tension force term. This force, upon discretization, is only non-zero across cells
 229 in which the level set function changes sign.

230 The interfacial curvature κ is computed with second order accuracy directly
 231 from the volume-of-fluid (VOF) function using the height function technique
 232 (Sussman [40], Sussman et al. [44]). We remark that we get the same results if
 233 we were to compute κ directly from the LS function using the “level set” height
 234 function technique.

235 Since ρ and μ are taken to be constant in each fluid, with a jump at the
 236 interface, they can be expressed in terms of the Heaviside function,

$$\rho = \rho_m \mathcal{H} + \rho_b (1 - \mathcal{H}), \quad \mu = \mu_m \mathcal{H} + \mu_b (1 - \mathcal{H}). \quad (6)$$

237 The subscripts “b” and “m” refer to “drop or bubble” and “matrix fluid”,
 238 respectively. To represent the free surface with the CLSVOF method, we must
 239 evolve the solution to both the VOF equation for F and the LS equation for ϕ :

$$\frac{\partial F}{\partial t} + (\mathbf{u} \cdot \nabla) F = 0, \quad \frac{\partial \phi}{\partial t} + (\mathbf{u} \cdot \nabla) \phi = 0. \quad (7)$$

240 In all computations the discretized variables p , ϕ and F are located at cell
 241 centers and the discrete variable \mathbf{u} is located at cell face centers. Our com-
 242 putations are performed using an overall second-order accurate hydrodynamic
 243 scheme. The spatial discretization uses second-order accurate, slope-limited,
 244 upwind techniques for the nonlinear advective terms. The velocity and pressure
 245 fields are computed using an implicit pressure projection procedure.

246 The temporal discretization of our numerical method is an operator split
 247 projection method as described by Sussman et al. [44]. An outline of our method
 248 is as follows (see Sussman et al. [44], section 4, for more details):

All Steps. Timestep

249 The timestep, Δt , is governed by the CFL condition and surface tension
 250 (section 5.7 of Sussman et al. [44]):

$$\Delta t < \min_{i,j,k} \left(\frac{\Delta x}{2|U^n|}, \frac{1}{2} \sqrt{\frac{\rho^L}{8\pi\sigma}} \Delta x^{3/2} \right)$$

Step 1. CLSVOF interface advection

$$\begin{aligned} \phi^{n+1} &= \phi^n - \Delta t [\mathbf{u} \cdot \nabla \phi]^n \\ F^{n+1} &= F^n - \Delta t [\mathbf{u} \cdot \nabla F]^n \end{aligned}$$

Step 2. Nonlinear advective force terms

$$\mathcal{A} = [\mathbf{u} \cdot \nabla \mathbf{u}]^n$$

Step 3. Viscosity force

$$\frac{\mathbf{u}^* - \mathbf{u}^n}{\Delta t} = -\mathcal{A} + g\vec{z} - [\nabla p/\rho]^n + \frac{1}{2} \frac{\nabla \cdot (2\mu \mathbf{D}^n) + \nabla \cdot (2\mu \mathbf{D}^*)}{\rho}$$

251 Step 4. Pressure projection and ghost fluid surface tension algorithm

$$\mathbf{V} = \mathbf{u}^n + \Delta t(-\mathcal{A} + g\vec{z} + \frac{1}{2} \frac{\nabla \cdot (2\mu \mathbf{D}^n) + \nabla \cdot (2\mu \mathbf{D}^*)}{\rho})$$

252

$$\mathbf{V} = \mathbf{V} - \Delta t \frac{\sigma \kappa(\phi^{n+1})}{\rho} \nabla \mathcal{H}(\phi^{n+1})$$

253

$$\nabla \cdot \frac{\nabla p}{\rho} = \frac{1}{\Delta t} \nabla \cdot \mathbf{V}$$

254

$$\mathbf{u}^{n+1} = \mathbf{V} - \Delta t \frac{\nabla p}{\rho}$$

255 To make efficient use of computational resources, our numerical simulations
 256 utilize an adaptive hierarchy of grids based on a dynamic adaptive mesh refine-
 257 ment (AMR) technique (Sussman et al. [41]). Adaptive grids are dynamically
 258 adjusted based on the location of the deforming gas-liquid interface. In the
 259 AMR technique the grid resolution is increased in regions near the interface
 260 while a coarser grid is used where the flow is relatively steady. The upper panel
 261 of Figure 1(b) displays a schematic view of the hierarchical grid structure and
 262 the lower panel corresponds to an actual computational example corresponding
 263 to bubble deformation in simple linear shear flow. In general, the mesh hier-
 264 archy is composed of different levels of refinement ranging from coarsest $\ell = 0$
 265 (“level-0”) to finest $\ell = \ell_{\max}$ (“level- ℓ_{\max} ”). The refinement ratio of one grid
 266 size ($\Delta x = \Delta y = \Delta z$) to the next finer level is two so that $\Delta x^{\ell+1} = 0.5 \Delta x^\ell$. All
 267 computations in this study used an AMR system with a maximum prescribed
 268 level $\ell_{\max} = 1$ (as illustrated in the upper panel of Figure 1(b)). In our adap-
 269 tive mesh refinement algorithm, the velocity in coarse grid cells that neighbor
 270 fine grid cells is interpolated from the coarse grid using bilinear interpolation in
 271 order to initialize “ghost” fine cells. Thus, the bilinear interpolation procedure
 272 produces interpolated fine grid data as a linear combination of the coarse grid
 273 data.

274 *3.2. Validation of the numerical method*

275 The effectiveness of our computational method has been demonstrated for
 276 the complicated rising motion of single bubbles and drops in viscous liquids
 277 Ohta and Sussman [29], Ohta et al. [26, 27] . In this section, the accuracy
 278 of our computational method will be verified for the problem of shear-induced
 279 deformation of a drop and bubble. First, we compare quantitatively against
 280 the steady-state drop deformation results reported by Li et al. [24]. The shape
 281 of a deformed drop in simple linear shear flow is described in terms of the Taylor
 282 deformation parameter $D=(a-b)/(a+b)$, where a and b are the major and minor
 283 axes of the deformed drop. For consistency, we perform numerical simulations
 284 using CLSVOF over the same computational domain and grid size used in Li
 285 et al. [24], which has dimensions $L(8R) \times W(4R) \times H(8R)$ (recall that R is the
 286 bubble/drop radius) and a level-0 grid size $\Delta x = \Delta y = \Delta z = R/8$; our two-level
 287 AMR grid structure also uses a finer level-1 grid size $\Delta x^{\ell=1} = \Delta y^{\ell=1} = \Delta z^{\ell=1} =$
 288 $R/16$. Numerical results are listed in Table 1 for D as a function of Re , with
 289 $Ca = 0.3$ and $\lambda = \eta = 1$ fixed in every case, obtained with the VOF method
 290 used in Li et al. [24], and also with our CLSVOF algorithm. Table 1 indicates
 291 that our numerical results are in good agreement with previous computations
 292 for drop deformation and breakup.

Table 1: Comparison of the Taylor deformation parameter D for a drop as a function of Re ($Ca = 0.3$, $\lambda = \eta = 1$). In all cases, the domain size is $L(8R) \times W(4R) \times H(8R)$, where R is the drop radius. CLSVOF method computations used a two-level AMR computational domain with a level-0 discretization $\Delta x^{\ell=0} = \Delta y^{\ell=0} = \Delta z^{\ell=0} = R/8$ and a level-1 discretization $\Delta x^{\ell=1} = \Delta y^{\ell=1} = \Delta z^{\ell=1} = R/16$.

Reynolds number	0.1	0.5	0.6	0.75
D (Li et al. [24])	0.3968	0.45	0.4768	Breakup
D (Our study)	0.3960	0.4570	0.4758	Breakup

292 Next, we examine the validation of our computational method in which we
 293 compare with the “bubble deformation in simple linear shear flow” results re-
 294 ported by Müller-Fischer et al. [25]. Müller-Fischer et al. [25] experimentally
 295 inquired into the bubble deformation under the condition of $Re \approx 0$. In our
 296 study, we computed the bubble deformation on a computational domain with
 297 dimensions $L(12R) \times W(6R) \times H(6R)$ and a computational grid in which the
 298 finest level grid size was $\Delta x^{\ell=1} = \Delta y^{\ell=1} = \Delta z^{\ell=1} = R/16$. Computations
 299 were performed for the conditions of $Ca = 0.96$ and $Ca = 1.63$ with $Re \approx 0$
 300 ($Re = 5.0 \times 10^{-4}$), $\lambda = 1.2 \times 10^{-3}$ and $\eta \leq 1.2 \times 10^{-6}$. The parameters
 301 that we have prescribed are consistent with the experimental conditions by
 302 Müller-Fischer et al. [25]. Comparisons of our numerical results and previous
 303 experimental results (Müller-Fischer et al. [25]) are tabulated in Table 2. Ad-
 304 ditionally, in Table 2, we also list experimental results with the condition of
 305 $Re \approx 0$ and $\lambda \approx \eta \approx 0$ by Rust and Manga [37]. These experimental values
 306 were obtained from the graph showing the relation of D vs Re (Rust and Manga
 307 [37]). As is clear from Table 2, our numerical results predicted larger values of
 308 D than the experimental results.

309 D than experimental ones reported by Müller-Fischer et al. [25]. Nevertheless,
 310 we found that our numerical results are very close to the experimental results
 311 by Rust and Manga [37], which emphasizes the intrinsic difficulties associated
 312 with experimental investigations of bubble dynamics, even in simple linear shear
 313 flow. These comparisons suggest that our computational method is effective and
 314 robust at reproducing bubble dynamics in simple linear shear flow.

Table 2: Comparison of D for a bubble as a function of Ca ($Re \approx 0$, $\lambda \approx \eta \approx 0$). In all cases, the domain size is $L(12R) \times W(6R) \times H(6R)$. CLSVOF computations used a two-level AMR computational domain with a level-0 discretization $\Delta x^{\ell=0} = \Delta y^{\ell=0} = \Delta z^{\ell=0} = R/8$ and a level-1 discretization $\Delta x^{\ell=1} = \Delta y^{\ell=1} = \Delta z^{\ell=1} = R/16$.

Capillary number	0.96	1.63
D (Müller-Fischer et al. [25])	0.37	0.58
D (Rust and Manga [37])	0.71 ± 0.05	0.81 ± 0.02
D (Our study $\Delta x^{\ell=1} = R/16$)	0.63	0.71

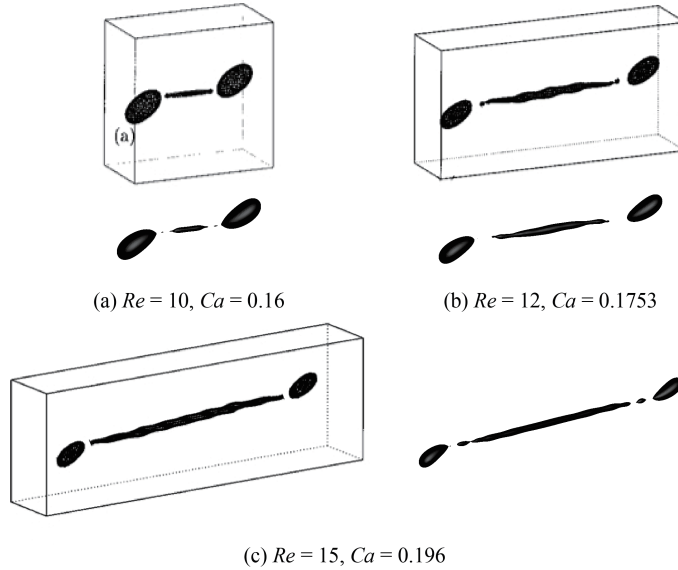


Figure 2: Comparison with results reported in Renardy and Cristini [36] (shown in boxes) for drop breakup in shear flow. In Renardy and Cristini [36], the computational domain dimensions were $W = 4R$, $H = 8R$, and L was varied depending on the Re and Ca conditions. The grid size in Renardy and Cristini [36] was set to $\Delta x = \Delta y = \Delta z = R/8$. Reprinted with permission from reference Renardy and Cristini [36]. Copyright 2001, AIP Publishing. Results obtained with our CLSVOF algorithm, corresponding to each case in reference Renardy and Cristini [36], are shown outside boxes. The CLSVOF method used a two-level AMR computational domain with a level-0 discretization $\Delta x^{\ell=0} = \Delta y^{\ell=0} = \Delta z^{\ell=0} = R/8$ and a level-1 discretization $\Delta x^{\ell=1} = \Delta y^{\ell=1} = \Delta z^{\ell=1} = R/16$. The onset of drop breakup is demonstrated for (a) $Re = 10$, $Ca = 0.16$, (b) $Re = 12$, $Ca = 0.1753$, and (c) $Re = 15$, $Ca = 0.196$. For all three Re and Ca conditions, $\lambda = \eta = 1$.

Finally, we present a comparison with numerical results for drop breakup reported in Renardy and Cristini [36]. Figure 2 demonstrates drop breakup with pinch-off behavior for three Re and Ca conditions and with constant values of $\lambda = \eta = 1$ for all cases. The three cases that we consider correspond to (a) $Re = 10, Ca = 0.16$, (b) $Re = 12, Ca = 0.1753$, and (c) $Re = 15, Ca = 0.196$, and which are illustrated in Figures 2(a)-(c), respectively. The results reported in Renardy and Cristini [36], which were obtained with a VOF method, are shown inside boxes while results obtained with our CLSVOF approach are displayed outside boxes. In the computations presented in Renardy and Cristini [36], the dimensions $W = 4R$ and $H = 8R$ were fixed, while L was changed depending on Re and Ca conditions, and the grid size was set to $\Delta x = \Delta y = \Delta z = R/8$. To compare with their results, we performed simulations with the CLSVOF method over a two-level AMR computational domain of the same dimensions and the same level-0 discretization: $\Delta x^{\ell=0} = \Delta y^{\ell=0} = \Delta z^{\ell=0} = R/8$; we set the finer level-1 grid size $\Delta x^{\ell=1} = \Delta y^{\ell=1} = \Delta z^{\ell=1} = R/16$. The results shown in Figure 2 verify that our numerical approach can reproduce the same drop breakup behavior presented in Renardy and Cristini [36]. Slight differences between the results can be attributed to the increased resolution used in our study in the level-1 grid around the elongated drop.

The numerical validation studies performed in this section and the following section demonstrate that our numerical method can reliably determine the transition regions at which shear-induced bubble or drop deformation leads to breakup. We remark that in the next section, we demonstrate that we can expect an error of 3% for predicting the transition to break-up. The analysis in this section and the following also demonstrate that the error is reduced by a factor of 2 each time the grid is refined by a factor of 2. Also, we refer the reader to Ohta et al. [28] in which we apply our CLSVOF method for bubble formation problems.

3.3. Consideration of domain and grid sizes

3.3.1. Selecting the appropriate domain size

The computational domain size used in numerical studies can affect the behavior of drop deformation and breakup. Referring to Figure 1(a), with an appropriately large domain length L and a fixed width $W = 4R$, the effect of the height H on drop behavior was examined in Li et al. [24] for Stokes flows and various Ca conditions and in Komrakova et al. [21] for $Re = 1$ and $Ca = 0.27$. Other related studies investigated drop breakup sensitivity (Renardy and Cristini [34]) and drop deformation sensitivity (Renardy et al. [35]) with respect to the entire domain size.

Here we investigate the drop dynamics sensitivity to domain size around the critical Reynolds number $Re_c = 0.75$. Specifically, we consider domain size sensitivity for the condition of $Re = 0.75, Ca = 0.3$, and $\lambda = \eta = 1$, which is a condition used in the comparison studies of the previous section. As shown in Table 1, the drop breaks up for the condition of $Re = 0.75$ and $Ca = 0.3$ with a domain size of $L(8R) \times W(4R) \times H(8R)$. Results for domain size sensitivity

Table 3: Comparison of the Taylor deformation parameter D for a drop as a function of domain size ($Re = 0.75$, $Ca = 0.3$, $\lambda = \eta = 1$). CLSVOF method computations used a two-level AMR computational domain with a level-0 discretization $\Delta x^{\ell=0} = \Delta y^{\ell=0} = \Delta z^{\ell=0} = R/8$ and a level-1 discretization $\Delta x^{\ell=1} = \Delta y^{\ell=1} = \Delta z^{\ell=1} = R/16$.

System	Domain size ($L \times W \times H$)	D
System 1	$8R \times 4R \times 8R$	Breakup
System 2	$12R \times 4R \times 8R$	Breakup
System 3	$8R \times 4R \times 6R$	0.541
System 4	$8R \times 6R \times 6R$	0.466
System 5	$8R \times 8R \times 8R$	0.460
System 6	$8R \times 16R \times 16R$	0.460

for six domain systems, all of which use a level-1 grid size $\Delta x^{\ell=1} = \Delta y^{\ell=1} = \Delta z^{\ell=1} = R/16$, are tabulated in Table 3. Note that the domain size used in the comparison study (Table 1) corresponds to System 1.

The results in Table 3 suggest that drop deformation is promoted when we use a domain size with $W = 4R$. In contrast, the drop does not break up and becomes stable with a deformed shape if we set L large enough and $W \geq 6R$ and $H \geq 6R$. Since the value of D for the domain size $L(8R) \times W(6R) \times H(6R)$ differs by only 1.3% with the value for the domain size of $L(8R) \times W(16R) \times H(16R)$, in the results that follow we set the width to $W = 6R$ and the height to $H = 6R$ to minimize the number of computational grid nodes along those directions. To determine the critical Reynolds number Re_c (with $Ca = 0.3$), we consider a domain size of $L(24R) \times W(6R) \times H(6R)$, and we find that the drop reaches a stable state with deformation parameter $D=0.549$ for $Re = 1.0$, while a value of $Re = 1.1$ leads to drop breakup.

3.3.2. Selecting the appropriate grid size

The grid size and adaptive meshing strategy that we adopt is chosen in order to answer the research question as to the conditions which determine whether a bubble in shear flow will break-up or not. In such a case, we must accurately capture the balance of forces with respect to the (non-local) force exerted from the wall driven flow acting against the interfacial surface tension force. The accuracy of the “Critical Reynolds Number” depends on the largest Taylor Deformation parameter D that is supported by the grid (see e.g. Figures 8 and 11). As we report here, we have found that as long as the grid size is fine enough to support a Taylor Deformation parameter $D < 0.95$, then the transition region (i.e. “Critical Reynolds number”) (see Figures 3 and 12) will be captured with a tolerance of three percent. The simulation time becomes impractical if we were to try to further improve the “critical Reynolds number” accuracy. A smaller tolerance would necessitate a larger supported Deformation parameter D which would in turn necessitate a higher aspect ratio computational domain, increased droplet surface area at break-up, increased number of time steps, and higher resolution for representing the drop/bubble at its thinnest point.

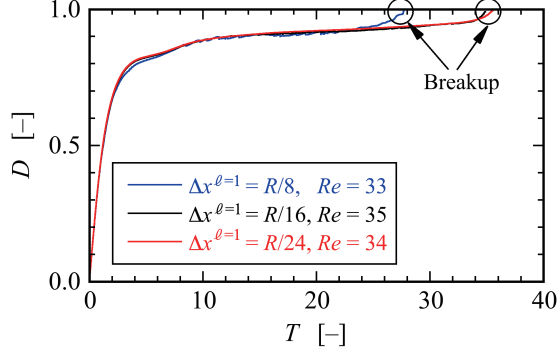


Figure 3: Time evolution of the deformation parameter D versus dimensionless time $T = \Gamma t$ for a bubble, obtained with three grid systems at different resolutions. All three resolutions use a two-level AMR grid with an effective fine resolution grid size $\Delta x^{\ell=1} = \Delta y^{\ell=1} = \Delta z^{\ell=1}$. The evolution of D using the first system, where $\Delta x^{\ell=1} = R/8$, is shown in blue and it predicts that bubble breakup occurs at a Reynolds number $Re = 33$. The evolution of D using the second system, where $\Delta x^{\ell=1} = R/16$, is shown in black and it predicts that bubble breakup occurs at a Reynolds number $Re = 35$. Results with the third system, shown in red, use $\Delta x^{\ell=1} = R/24$, and they predict that breakup occurs at $Re = 34$. The capillary number corresponding to these results is $Ca = 1.0$. ($\lambda = 1.2 \times 10^{-3}$, $\eta < 1.0 \times 10^{-3}$)

390 We make the distinction between our present research, and the research
 391 found in the work of Zhang et al. [55, 56] on predicting the conditions for bubble
 392 mergers. Even in the most extreme cases for mergers, the largest Deformation
 393 parameter never exceeds 0.4 in Zhang et al. [55]. In summary, our gridding
 394 requirements necessitate grid points distributed relatively evenly throughout the
 395 computational domain when a bubble is stretched to a $D = 0.9$ Deformation,
 396 whereas in Zhang et al. [55] the gridding strategy necessitates a more localized
 397 strategy.

398 The numerical results presented in this and the previous section used a
 399 finest-level grid size set to $\Delta x^{\ell=1} (= \Delta y^{\ell=1} = \Delta z^{\ell=1}) = R/16$. To verify the
 400 adequacy of this grid resolution, we present grid refinement results for a bubble
 401 breakup simulation with $Ca = 1.0$, which corresponds to the most deformable
 402 and stretchable bubble case considered in our numerical studies. We use three
 403 different grid systems, (i) $\Delta x^{\ell=1} = R/8$, (ii) $\Delta x^{\ell=1} = R/16$, and (iii) $\Delta x^{\ell=1} =$
 404 $R/24$, in order to determine Re_c . Figure 3 shows the time evolution of the
 405 deformation parameter D over time for the three grid systems; the x -axis is a
 406 dimensionless time defined by $T = \Gamma t$ and the y -axis is D . The results show that
 407 bubble breakup occurs at $Re_c = 35$ for the grid system with $\Delta x^{\ell=1} = R/16$,
 408 while the finer computational grid with $\Delta x^{\ell=1} = R/24$ predicts a critical value of
 409 $Re_c = 34$. For the $\Delta x^{\ell=1} = R/8$ results, it is clear that the $R/8$ resolution is too
 410 coarse in order to capture the proper break-up time, albeit the critical Reynolds'
 411 number, $Re_c = 33$, was still close to the finer grid resolution cases. Note that
 412 although the time evolution of D for the two finer resolution systems ($R/16$ and
 413 $R/24$) is consistent between the two, (the predicted critical Reynolds numbers

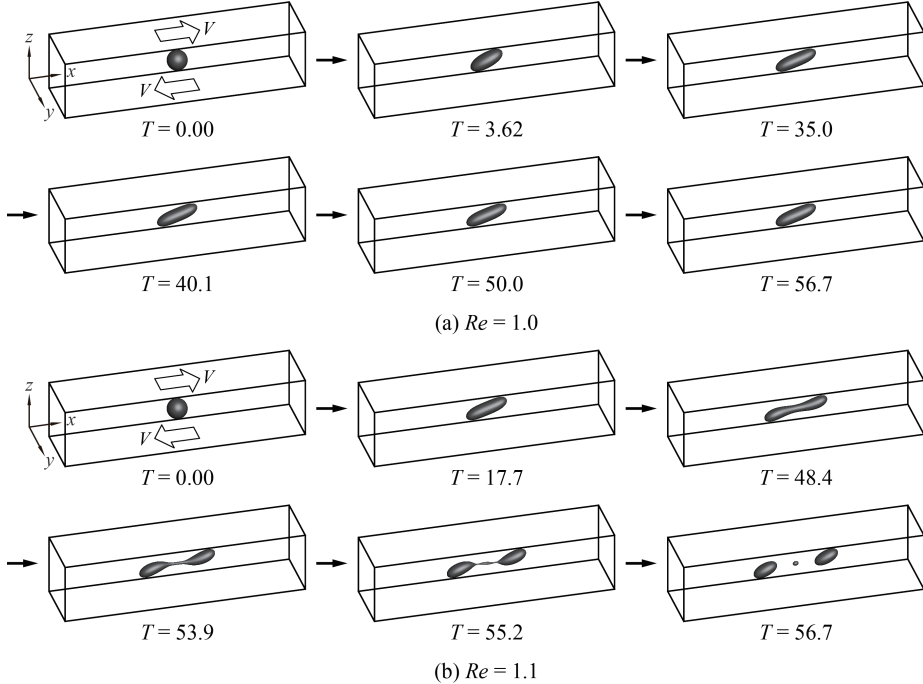


Figure 4: Time evolution of drop deformation and breakup in shear flow at the condition of $Ca = 0.3$ with (a) $Re = 1.0$ and (b) $Re = 1.1$. The “drop” critical Reynolds number corresponding to $Ca = 0.3$ is $1.0 < Re_c < 1.1$. ($\lambda = \eta = 1.0$)

differ by $\sim 3\%$), the computational time using the grid system with $\Delta x^{\ell=1} = R/24$ was more than 6 times longer than the one based on the coarser system with $\Delta x^{\ell=1} = R/16$. We remark that in our search for Re_c , we considered a wide range of values of Ca and we found it necessary to use a large L ($\sim 24R$) since for certain shear flows the bubble can stretch significantly without breaking up. Nevertheless, for the conditions presented in this section, the results indicate that our numerical approach, even with a finest-level resolution set to $\Delta x^{\ell=1} = R/16$, is capable of accurately reproducing bubble deformation and breakup without sacrificing any essential dynamical features.

4. Results and Discussion

4.1. Drop deformation and breakup

To illustrate the differences in deformation and breakup between a drop and a bubble around critical conditions, we first present numerical results for drop deformation. The time evolution of drop deformation and breakup in simple linear shear flow for two conditions is shown in Figure 4; the first case, shown in Figure 4(a), uses $Ca = 0.3$ and $Re = 1.0$, while the second case, depicted in Figure 4(b), uses $Ca = 0.3$ and $Re = 1.1$. Using a domain size of

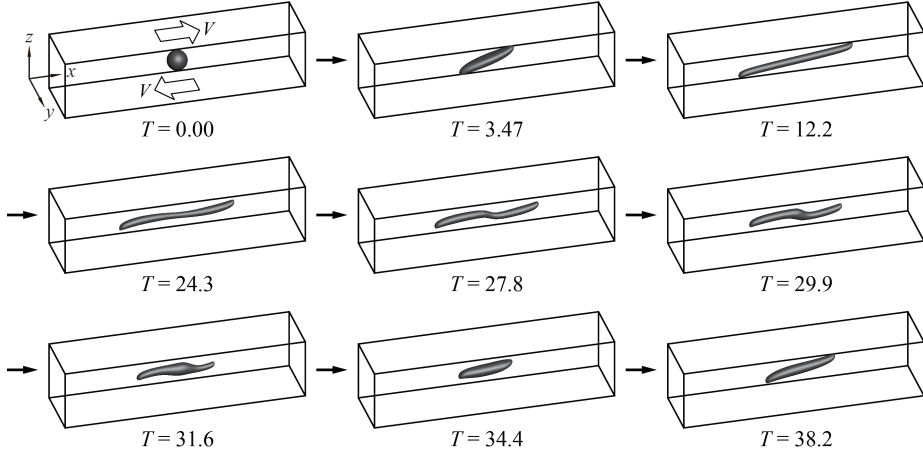


Figure 5: Time evolution of bubble deformation in shear flow at the condition of $Ca = 0.3$ and $Re = 92$. The “bubble” critical Reynolds number corresponding to $Ca = 0.3$ is $92 < Re_c < 93$. In contrast to the drop deformation case, when Re is slightly below Re_c (See Figure 4.1 $Re = 1.0$ for the drop case), the bubble shape will not reach a steady shape, instead the bubble shape alternates between the shapes “slightly stretched” ($T = 3.47$), fully stretched and “doglegged” ($T = 27.8$) and “almost” back to the original “slightly stretched” case ($T = 34.4$). ($\lambda = 1.2 \times 10^{-3}$, $\eta < 1.0 \times 10^{-3}$)

431 $L(24R) \times W(6R) \times H(6R)$, in the case with $Re = 1.0$, the drop gradually deforms
 432 and finally attains a stable deformed state. After $T = 35.0$, the drop remains a
 433 **stable deformed state with $D = 0.549$** . Over the same domain, for the case with
 434 $Re = 1.1$, the “mother” drop elongates over time and the volume at the ends
 435 of the deforming drop expands; that is, both ends of the drop become bulb-
 436 shaped. As time progresses, particularly over the time interval $48.4 \leq T \leq 55.2$,
 437 a thread-bridge forms between the bulbous ends and the thread-bridge becomes
 438 thinner. Finally, at around the dimensionless time $T \sim 56.7$, the mother drop
 439 breaks up, forming two “daughter” drops through the pinch off; one satellite
 440 drop is also generated between the pinched off daughter drops.

441 4.2. Bubble deformation and breakup

442 Next we present numerical results that illustrate the conditions that lead
 443 to bubble deformation without breakup as well as conditions where the bubble
 444 deforms and ultimately breaks up. The time evolution of shear-induced bubble
 445 deformation without breakup at the condition of $Ca = 0.3$ and $Re = 92$ is
 446 depicted in Figure 5 and the bubble breakup process with flow condition of
 447 $Ca = 0.3$ and $Re = 93$ is illustrated in Figure 6. The results indicate that
 448 the critical Reynolds number is approximately $Re_c = 93$ (with $Ca = 0.3$).
 449 A comparison with the drop breakup dynamics presented in Section 4.1 and
 450 the corresponding processes for bubble deformation and breakup exhibit very
 451 distinct features. First, we note that a relatively large shear force magnitude is
 452 required for bubble breakup ($\lambda = 1.2 \times 10^{-3}$, $\eta < 1.0 \times 10^{-3}$) compared with the

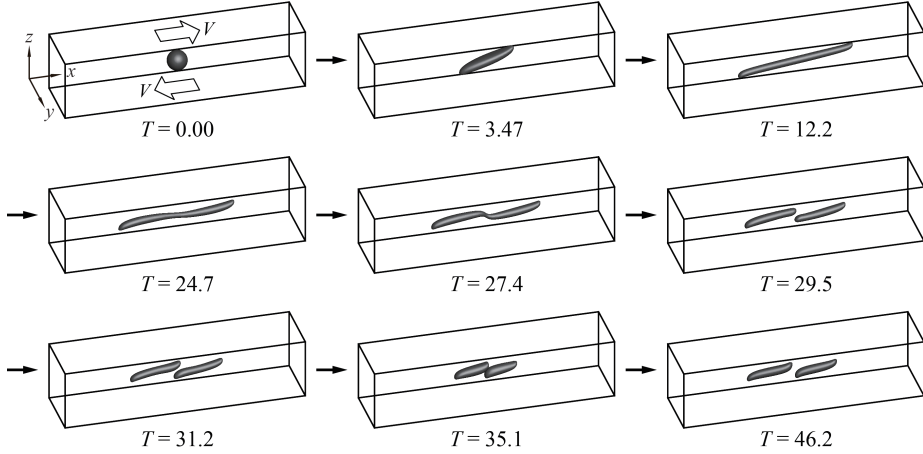


Figure 6: Time evolution of bubble deformation in shear flow at the condition of $Ca = 0.3$ and $Re = 93$. The “bubble” critical Reynolds number corresponding to $Ca = 0.3$ is $92 < Re_c < 93$. ($\lambda = 1.2 \times 10^{-3}$, $\eta < 1.0 \times 10^{-3}$)

case of the drop ($\lambda = \eta = 1$). Then, for the same value of $Ca = 0.3$, the critical Reynolds number for the bubble is around 85 times larger than that for the drop. Focusing on the bubble dynamics with no-breakup (Figure 5), the results show that the bubble is largely elongated in the x -direction at the early stages ($T \leq 24.3$) of bubble deformation, but the bubble does not develop the bulb-like shape (large volume areas) at both ends present in the drop deformation process. It is also evident that the ends of the deforming bubble develop cusped shapes under the influence of the strong shear flow. In providing a more detailed description, very large shear forces are required to deform the bubble because $\lambda \simeq 0$ and $\eta \simeq 0$. Thus, the bubble undergoing large shear forces at $T > 0$ is largely stretched long the shear flow direction, and the very long elongated bubble with cusped shapes is formed. Accordingly, the bubble finally breaks up through f the elongated shape without forming a bulb-like shape. A noteworthy feature for the non-breaking bubble is that it does not settle into a deformed stable state as in the case of drop deformation presented in Figure 4.1(a). After an initial elongation process, the bubble enters a shrinking phase ($T = 27.8$) where the doglegged shape formed at the center of the bubble returns to a smaller deformed shape ($T = 34.4$) that is similar to its earlier shape ($T = 34.7$). However, when we compare the early deformed bubble shape at $T = 34.7$ with the shape at $T = 34.4$, it is clear that the shapes are not identical. Following the shrinking phase, the bubble begins to stretch again ($T = 38.2$) and the bubble oscillates between its elongated shape and shortened geometry.

For the case of bubble breakup (Figure 6), we observe that the deformation process is almost the same as the no-breakup case until the doglegged shape is formed at $T \sim 27.4$. The bubble finally breaks during the time interval $27.7 \leq T \leq 29.5$. For a closer examination of the bubble breakup process,

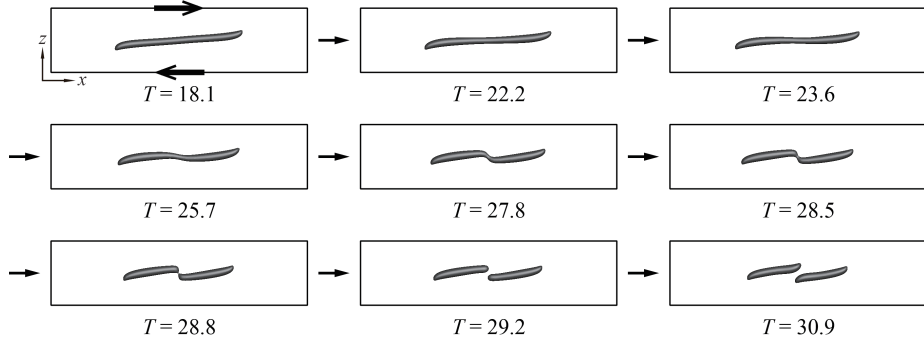


Figure 7: Detail of bubble breakup process in shear flow at the condition of $Ca = 0.3$ and $Re = 93$. The “bubble” critical Reynolds number corresponding to $Ca = 0.3$ is $92 < Re_c < 93$. ($\lambda = 1.2 \times 10^{-3}$, $\eta < 1.0 \times 10^{-3}$)

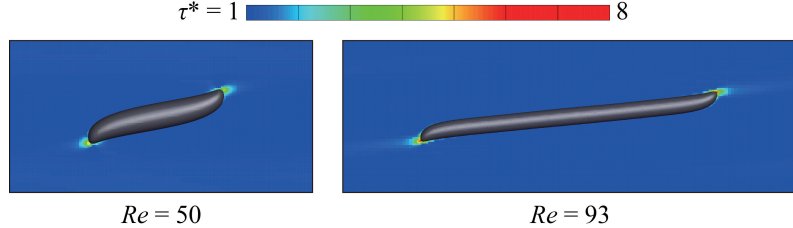


Figure 8: Normalized shear stress τ^* around a bubble for two Reynolds numbers under the condition of $Ca = 0.3$. The left image shows the shear stress profile at $Re = 50$ and the right image at $Re = 93$.

479 a detailed panel of cross-sectional slices in the xz -plane through the bubble
 480 shape center is presented in Figure 7. The images displayed in Figure 7, which
 481 are taken at shorter time intervals than those shown in Fig. 6, reveal that the
 482 bubble breaks up into two daughter bubbles due to the pinch off at the thread-
 483 bridge part of the doglegged shape during the shrinking process ($T = 28.5 \sim$
 484 28.8). After breaking up, the two daughter bubbles migrate to the center: the
 485 left daughter bubble moves toward the right-side of the domain and the right
 486 daughter bubble moves to the left side (see results for $T = 29.5 \sim 35.1$ in
 487 Figure 6 and for $T = 28.8 \sim 30.9$ in Figure 7). The two daughter bubbles then
 488 momentarily congregate near the domain center ($T = 35.1$ in Figure 6), before
 489 they slowly start to separate: the left daughter bubble moves to the left and the
 490 right daughter bubble moves to the right ($T = 46.2$ in Figure 6). The results
 491 clearly demonstrate that the bubble breakup process is markedly different from
 492 the analogous drop breakup process with $\lambda = 1$ and $\eta = 1$. Note that the
 493 appearance of deformation and breakup of the drop will largely depend on the
 494 viscosity ratios.

495 *4.3. Shear stress acting on the bubble*

496 In the previous section, the appearance of bubble deformation and breakup
497 was discussed. It is expected that a large deformation and breakup of the bubble
498 are closely related to the state of shear stress acting on the bubble. Figure 8
499 shows the shear stress profile around a bubble for two Reynolds numbers under
500 the condition of $Ca = 0.3$: Reynolds number equal to 50 and 93. The shear
501 stress profile on the left corresponds to the case of $Re = 50$ and the right side
502 shows the shear stress profile for the case of $Re = 93$. The normalized shear
503 stress, $\tau^* = \tau/\tau_0$, is defined as a ratio of the local shear stress $\tau = \mu_m \sqrt{2\mathbf{D} : \mathbf{D}}$
504 and the apparent shear stress $\tau_0 = \mu_m \Gamma$. In this study, for a given Ca condition,
505 the same value of τ_0 is used regardless of Re . For the case of $Re = 50$, the bubble
506 reached a deformed stable state, **and the shear stress profile around the bubble
507 was drawn after the bubble attained a stable deformed state.** As observed
508 in previous sections, when the value of Re is slightly below the critical Re
509 condition, the bubble does not settle into a deformed stable state but instead
510 alternates in an elongation and contraction process. **The shear stress profile for
511 the case of $Re = 93$ was depicted when the bubble sufficiently elongated ($T =$
512 14.9).** In comparison to the $Re = 50$ case on the left, the right image in Fig. 8
513 ($Re = 93$) shows a higher shear stress profile near the bubble endpoints as it
514 undergoes an elongation state in the process toward breakup. The value of the
515 maximum shear stress for the case of $Re = 50$ is $\tau^* \approx 6$ and the maximum shear
516 stress for the case of $Re = 93$ at the moment shown in Fig. 8 has the value of
517 $\tau^* \approx 8$. The shear stress profile in Fig. 8 (color contour) is drawn in the range
518 from $\tau^* = 1$ to $\tau^* = 8$, but, for emphasis, shear stress regions with $\tau^* \geq 6$ are
519 illustrated in red. As can be seen in the figure, the strongest shear stresses are
520 concentrated on the ends of the bubble for both Re conditions. This indicates
521 that the strong shear stresses acting on the ends of the bubble are responsible
522 for much of the bubble stretching. It is important to note that the magnitude
523 of the shear stress acting on the ends of the bubble for the case of $Re = 93$ is
524 much larger than that for the case of $Re = 50$.

525 We also observe that the shear stress inside the bubble was very small relative
526 to that of the matrix fluid due to very small density and viscosity of the bubble.
527 Since the force of strong shear stresses acting on the ends of the bubble is
528 difficult to transfer across the interface, as a consequence, a sufficiently large Re
529 condition is required for large bubble deformations.

530 In summary, what we discover is that for the Reynolds number sufficiently below
531 the critical value, a relatively quick unsteady elongation period gives way to a
532 steady state (with no break up). On the other hand for Reynolds number close
533 to the critical Reynolds number, there is a prolonged, unsteady, elongation
534 period, in which periodic motion is observed and the deformation parameter
535 D is close to one. The “vacillating” behavior cannot last forever, ultimately
536 (perhaps stochastically!), the bubble will either settle down or break. We assert
537 that regardless of the outcome, this vacillating behaviour will always occur in
538 close proximity to the critical Reynolds’ number. In other words, regardless of
539 the outcome, we claim, using the grid resolution of $R/16$, that one is assured
540 of being within 3 percent of the critical Reynolds number (see Figure 3). In

541 fact, we hypothesize that there will always be “vacillating” behavior if one is
 542 sufficiently close to the critical Reynolds number. i.e. given an almost infinite
 543 supply of computational resources, as one hones in closer and closer to the
 544 critical Reynolds number, a “tug of war” will be observed between the surface
 545 tension force trying to pull the bubble together versus the wall driven shear
 546 stress trying to pull the bubble apart.

547 *4.4. Velocity field outside and inside the breaking bubble*

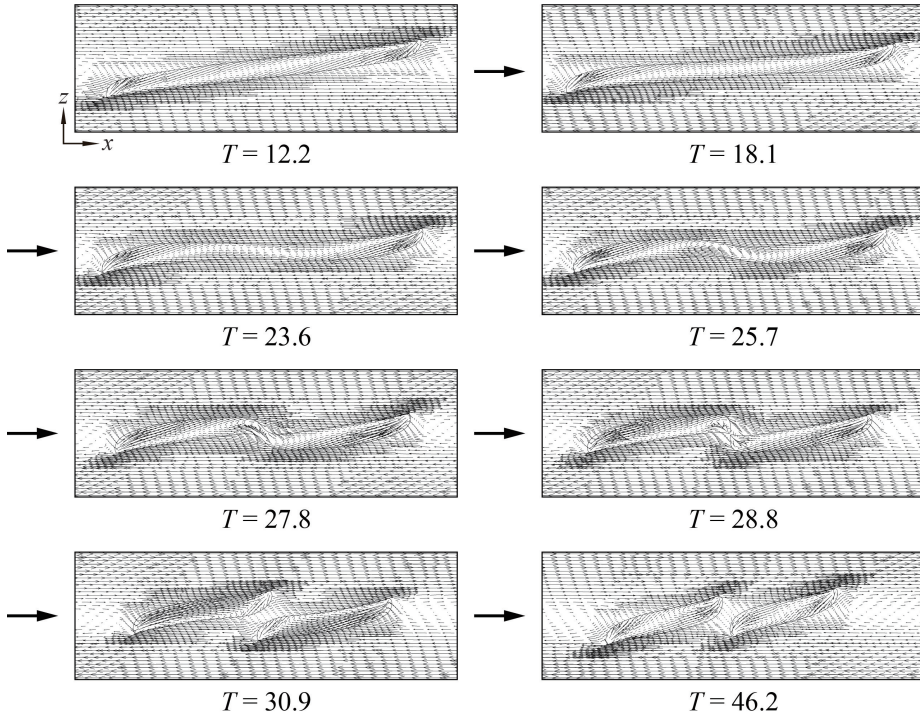


Figure 9: Fluid velocity field outside and inside the breaking bubble in shear flow at the condition $Ca = 0.3$ and $Re = 93$. The “bubble” critical Reynolds number corresponding to $Ca = 0.3$ is $92 < Re_c < 93$. ($\lambda = 1.2 \times 10^{-3}$, $\eta < 1.0 \times 10^{-3}$)

548 In this section, we consider the fluid flow velocity field outside and inside the
 549 bubble during the shear-induced breakup process. **Detailed velocity fields of the**
 550 **deforming and breaking drop have already been presented in some references**
 551 **(Li et al. [24], Renardy and Cristini [34]).** The velocity fields for the drop and
 552 the bubble will be influenced by the behavior of the breakup process, so the
 553 velocity fields for the drop and the bubble are not similar. Figure 9 shows the
 554 velocity fields outside and inside the bubble at cross-sectional slices in the xz -
 555 plane for a flow condition of $Ca = 0.3$ and $Re = 93$. Regions around the bubble
 556 where there is a higher density of velocity vectors correspond to the level-1 grid
 557 portion of the AMR structure. The simulation results show that the velocity

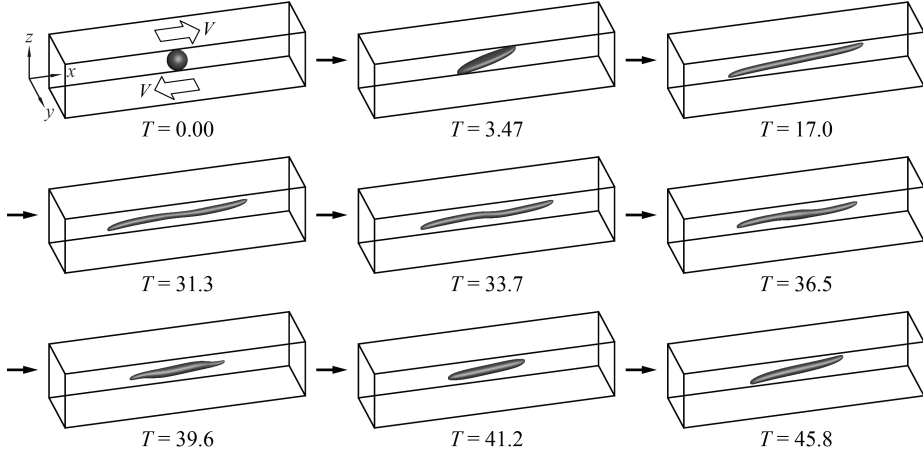


Figure 10: Time evolution of bubble deformation in shear flow at the condition of $Ca = 0.8$ and $Re = 42$. The “bubble” critical Reynolds number corresponding to $Ca = 0.8$ is $42 < Re_c < 43$. ($\lambda = 1.2 \times 10^{-3}$, $\eta < 1.0 \times 10^{-3}$)

field inside the bubble is particularly distinct from the surrounding flow field in the exterior of the bubble. The cross-sections at $T = 12.2$ and $T = 18.1$, taken during the elongation phase, show how shear forces at the lower and upper halves of the bubble act along the bottom and top surfaces, respectively, to deform the interface. Near the left and right edges of the bubble, inward interior flows (that point toward the bubble center) begin to develop. Strong shearing forces in the exterior near the bottom-left-end and top-right-end of the bubble interact with the interior flow field through the boundary to create cusped shapes at the bottom-left and top-right ends of the bubble while the interface is laterally elongated in the x -direction. During the shrinking process, which occurs for $23.6 \leq T \leq 27.8$, inward flows within the bubble extend over a wider region and are no longer localized near the bubble edges. Then, we observe that circulating flows form at the thread-bridge part of the doglegged bubble shape over the time interval [25.7, 27.8]. During the breakup process ($T \sim 28.8$), higher-intensity inward flows are formed inside the bubble, near the pinch off region, that are naturally larger than the surrounding interior flows and which are inextricably associated with the bubble migration illustrated in Figs. 6 and 7. As time proceeds further ($T = 46.2$), distinct inward flows are formed inside the daughter bubbles; the bubbles then begin their migration toward the side walls. Considering the left daughter bubble, for example, we see that the mechanism responsible for this movement results from larger shear forces acting on the bottom-left end than those in the top-left end.

4.5. Effect of surface tension on bubble deformation and breakup

In previous sections, we considered numerical simulations of bubble deformation and breakup with a capillary number $Ca = 0.3$. Here, we examine

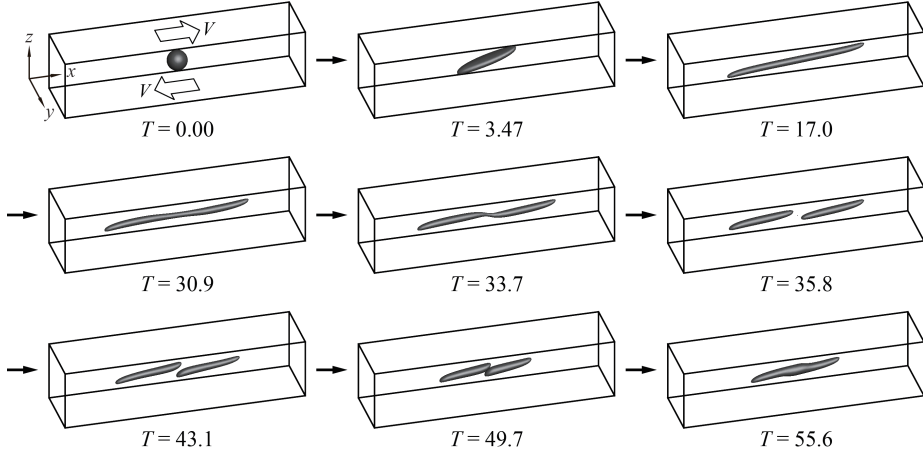


Figure 11: Time evolution of bubble deformation in shear flow at the condition of $Ca = 0.8$ and $Re = 43$. The “bubble” critical Reynolds number corresponding to $Ca = 0.8$ is $42 < Re_c < 43$. ($\lambda = 1.2 \times 10^{-3}$, $\eta < 1.0 \times 10^{-3}$)

similar bubble dynamics with $Ca = 0.8$ and we also investigate the effect of interfacial tension on bubble deformation and breakup. Using $Ca = 0.8$ for both cases, Figures 10 and 11 present the time evolution of shear-induced bubble deformation and breakup with $Re = 42$ and $Re = 43$, respectively. We note that the bubble critical Reynolds number is around $Re_c \approx 43$, whereas $Re_c \approx 0$ for the corresponding case of the drop with $\lambda = \eta = 1$ (see e.g. Li et al. [24]). Note that Re_c for $Ca = 0.8$ is smaller than that for the condition of $Ca = 0.3$ since the bubble at $Ca = 0.8$ is more elastic due to the weaker effect of surface tension in this case. The results shown in Figs. 10 and 11 indicate that the bubble deformation and breakup process for the condition of $Ca = 0.8$ is analogous to that for $Ca = 0.3$. For the case of bubble deformation without breakup (Fig. 10), the bubble initially assumes a long elongated shape along the x -direction at around $T = 17.0$. The bubble then enters a compression stage over the time interval $[31.3, 41.2]$ and subsequently starts to elongate again at $T = 45.8$. On the other hand, for the case of bubble breakup (Fig. 11), an initial elongation phase is followed by a doglegged shape formation at $T = 33.7$. After that, the bubble ruptures from the thread-bridge part of the doglegged shape and two daughter bubbles are produced ($T = 35.8$). The two daughter bubbles formed after breakup move to the central area ($T = 49.7$) as in the case of $Ca = 0.8$ and $Re = 93$, but the two bubbles eventually coalesce in a region approximately centered in the computational domain ($T = 55.6$). We note that in a real experimental setting, bubbles may coalesce after breaking up due to slight deviations of flow conditions and states. Although the process of bubble deformation and breakup for flow conditions with $Ca = 0.3$ and $Ca = 0.8$ are similar, a pronounced difference is that the bubble for $Ca = 0.8$ is more elongated and slender than that for $Ca = 0.3$ due to the smaller effect of surface

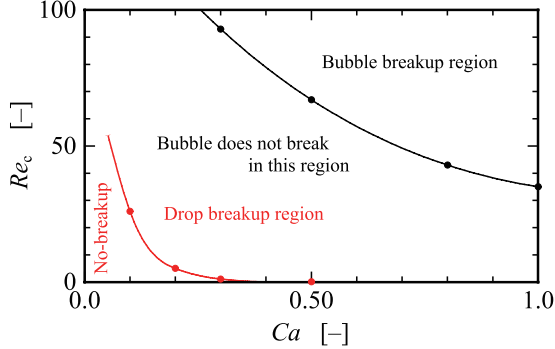


Figure 12: A plot of the critical Reynolds number versus capillary number for the data listed in Table 4. $\lambda = 1.2 \times 10^{-3}$, $\eta < 1.0 \times 10^{-3}$, $0.3 < Ca < 1$, and the initial/boundary conditions are given by (1). Given a new data point, (Ca, Re) , one can reliably predict whether the given (Ca, Re) pair will result in shear induced bubble break-up or not. Note, for the “Drop delineation curve,” $\lambda = \eta = 1$.

609 tension for $Ca = 0.8$.

610 Table 4 lists, for representative Ca values, the corresponding critical Reynolds
 611 number, Re_c , for shear-induced bubble breakup. The data in Table 4 corre-
 612 sponds to $\lambda = 1.2 \times 10^{-3}$, $\eta < 1.0 \times 10^{-3}$, $0.3 < Ca < 1$, and the initial/boundary
 613 conditions are given by (1). The results in Table 4 indicate that sufficiently large
 614 shear forces are required for bubble breakup even for large capillary numbers.
 615 In Figure 12 we plot the smooth interpolant of the data given in Table 4 and
 616 make the hypothesis that given a new data point, (Ca, Re) , shear induced bub-
 617 ble break up will occur if the point (Ca, Re) is above the given critical curve,
 618 and the bubble will not break if the (Ca, Re) pair is below the critical curve.
 619 For comparison, a critical curve for the drop with $\lambda = \eta = 1$ is also indicated
 620 in Fig. 12. The inclusion of breakup and no-breakup critical curves, for both
 621 the drop and the bubble, will facilitate future identification of Re_c numbers—
 622 and thus a more complete general critical curve—for a wide range of high Ca
 623 numbers.

Table 4: Shear-induced bubble breakup for various flow conditions described in terms of column pairs of critical Reynolds numbers and corresponding capillary numbers. ($\lambda = 1.2 \times 10^{-3}$, $\eta < 1.0 \times 10^{-3}$)

	Capillary number Ca	0.3	0.5	0.8	1.0
Critical Reynolds number Re_c	93	67	43	35	

624 5. Conclusions

625 The bubble deformation and breakup process in simple linear shear flow
 626 liquid was explored numerically using the CLSVOF computational method. In

627 this study, the critical Reynolds number Re_c , at which bubble breakup first
628 occurs, was determined for several flow conditions, and the differences between
629 bubble deformation and breakup were compared with the well-known analogous
630 process of drop deformation and breakup.

631 Numerical results revealed significant differences between bubble deformation
632 and breakup and the corresponding drop dynamics. For case of bubble,
633 it was discovered that much stronger shear flows are necessary to induce in-
634 terface breakup compared with a drop immersed in a similar flow field. That
635 is, a much larger Reynolds number flow is required in order to induce bubble
636 breakup. The behavior of bubble breakup was very similar through the Ca
637 number range considered in our computations: the bubble underwent a simi-
638 lar breakup mechanism in which rupture occurred at a thread-bridge part that
639 followed a doglegged shape formation stage. In bubble deformation without
640 breakup, near Re_c , the bubble did not maintain a stable deformed shape, in
641 contrast to drop deformation near the critical Reynolds number. The bubble
642 exhibited pronounced underdamped behavior: the bubble oscillated between
643 elongating and shrinking motions for non-rupturing flow conditions. **At the**
644 **same time, bubble deformation under smaller Re conditions ($< Re_c$) becomes**
645 **in a stable state.** We attribute the large differences in morphology for the
646 bubble undergoing breakup, compared with the drop, to the density and viscos-
647 ity ratio. The density and viscosity ratio remarkably impacts on bubble/drop
648 deformation and breakup. The bubble deformation and breakup is subject to a
649 synergistic coupling of the density and viscosity ratio, and whose effect will be
650 examined separately in future work.

651 **References**

- 652 [1] Amani, A., Balcázar, N., Castro, J., Oliva, A., 2019. Numerical study of droplet deformation in shear flow using a con-
653 servative level-set method. *Chemical Engineering Science* 207,
654 153–171. URL: <http://www.sciencedirect.com/science/article/pii/S0009250919305123>, doi:<https://doi.org/10.1016/j.ces.2019.06.014>.
- 655 [2] Bazhlekov, I.B., Anderson, P.D., Meijer, H.E., 2006. Numerical investi-
656 gation of the effect of insoluble surfactants on drop deformation and
657 breakup in simple shear flow. *Journal of Colloid and Interface Sci-
658 ence* 298, 369 – 394. URL: <http://www.sciencedirect.com/science/article/pii/S0021979705012658>, doi:<http://dx.doi.org/10.1016/j.jcis.2005.12.017>.
- 659 [3] Bento, D., Rodrigues, R.O., Faustino, V., Pinho, D., Fernandes, C.S.,
660 Pereira, A.I., Garcia, V., Miranda, J.M., Lima, R., 2018. Deforma-
661 tion of red blood cells, air bubbles, and droplets in microfluidic devices:
662 Flow visualizations and measurements. *Micromachines* 9, 151. URL:
663 <https://www.mdpi.com/2072-666X/9/4/151>, doi:10.3390/mi9040151.

- 669 [4] Chu, P., Finch, J., Bournival, G., Ata, S., Hamlett, C., Pugh, R.J.,
670 2019. A review of bubble break-up. *Advances in Colloid and Interface
671 Science* 270, 108–122. URL: <https://www.sciencedirect.com/science/article/pii/S0001868619300211>, doi:<https://doi.org/10.1016/j.cis.2019.05.010>.
- 674 [5] Cristini, V., Bławzdziewicz, J., Loewenberg, M., 2001. An adaptive
675 mesh algorithm for evolving surfaces: simulations of drop breakup
676 and coalescence. *Journal of Computational Physics* 168, 445 –
677 463. URL: <http://www.sciencedirect.com/science/article/pii/S0021999101967130>, doi:<http://dx.doi.org/10.1006/jcph.2001.6713>.
- 679 [6] Cristini, V., Guido, S., Alfani, A., Bławzdziewicz, J., Loewenberg, M.,
680 2003. Drop breakup and fragment size distribution in shear flow. *Journal
681 of Rheology* 47, 1283–1298. URL: <http://scitation.aip.org/content/sor/journal/jor2/47/5/10.1122/1.1603240>, doi:<http://dx.doi.org/10.1122/1.1603240>.
- 684 [7] Croce, R., Griebel, M., Schweitzer, M.A., 2010. Numerical simulation of
685 bubble and droplet deformation by a level set approach with surface tension
686 in three dimensions. *International Journal for Numerical Methods in Fluids*
687 62, 963–993. URL: <http://dx.doi.org/10.1002/fld.2051>, doi:<10.1002/fld.2051>.
- 689 [8] Drenckhan, W., Saint-Jalmes, A., 2015. The science of foaming. *Advances
690 in Colloid and Interface Science* 222, 228–259. URL: <https://www.sciencedirect.com/science/article/pii/S0001868615000603>,
691 doi:<https://doi.org/10.1016/j.cis.2015.04.001>. Reinhard Miller,
692 Honorary Issue.
- 694 [9] Eftekhari, M., Schwarzenberger, K., Heitkam, S., Eckert, K.,
695 2021a. Interfacial flow of a surfactant-laden interface under asymmetric
696 shear flow. *Journal of Colloid and Interface Science* 599,
697 837–848. URL: <https://www.sciencedirect.com/science/article/pii/S0021979721006457>, doi:<https://doi.org/10.1016/j.jcis.2021.04.126>.
- 700 [10] Eftekhari, M., Schwarzenberger, K., Heitkam, S., Javadi, A.,
701 Bashkatov, A., Ata, S., Eckert, K., 2021b. Interfacial behavior
702 of particle-laden bubbles under asymmetric shear flow. *Langmuir* 37,
703 13244–13254. URL: <https://doi.org/10.1021/acs.langmuir.1c01814>,
704 arXiv:<https://doi.org/10.1021/acs.langmuir.1c01814>. pMID:
705 34726918.
- 707 [11] Ervin, E., Tryggvason, G., 1997. The rise of bubbles in a vertical shear
708 flow. *Journal of Fluids Engineering* 119(2), 443–449.

- 709 [12] Hernandez, F.H., Rangel, R.H., 2017. Breakup of drops in simple
 710 shear flows with high-confinement geometry. Computers & Fluids 146,
 711 23 – 41. URL: <http://www.sciencedirect.com/science/article/pii/S0045793017300038>, doi:<https://doi.org/10.1016/j.compfluid.2017.01.001>.
- 714 [13] Hirt, C., Nichols, B., 1981. Volume of fluid (vof) method
 715 for the dynamics of free boundaries. Journal of Computational
 716 Physics 39, 201 – 225. URL: <http://www.sciencedirect.com/science/article/pii/0021999181901455>, doi:[http://dx.doi.org/10.1016/0021-9991\(81\)90145-5](http://dx.doi.org/10.1016/0021-9991(81)90145-5).
- 719 [14] Inamuro, T., 2006. Lattice boltzmann methods for viscous fluid flows and
 720 for two-phase fluid flows. Fluid Dynamics Research 38, 641. URL: <http://stacks.iop.org/1873-7005/38/i=9/a=A04>.
- 722 [15] Inamuro, T., Tomita, R., Ogino, F., 2003. Lattice boltzmann simulations
 723 of drop deformation and breakup in simple shear flows. International
 724 Journal of Modern Physics B 17, 21–26. URL: <http://www.worldscientific.com/doi/abs/10.1142/S0217979203017035>, doi:10.
 725 1142/S0217979203017035.
- 727 [16] Ioannou, N., Liu, H., Zhang, Y., 2016. Droplet dynamics
 728 in confinement. Journal of Computational Science 17, 463 –
 729 474. URL: <http://www.sciencedirect.com/science/article/pii/S1877750316300308>, doi:<https://doi.org/10.1016/j.jocs.2016.03.009>. discrete Simulation of Fluid Dynamics 2015.
- 732 [17] Janssen, P., Anderson, P., 2008. A boundary-integral model for
 733 drop deformation between two parallel plates with non-unit viscosity
 734 ratio drops. Journal of Computational Physics 227, 8807–
 735 8819. URL: <http://www.sciencedirect.com/science/article/pii/S002199910800346X>, doi:<http://dx.doi.org/10.1016/j.jcp.2008.06.027>.
- 738 [18] Janssen, P.J.A., Anderson, P.D., 2007. Boundary-integral method
 739 for drop deformation between parallel plates. Physics of Fluids
 740 19. URL: <http://scitation.aip.org/content/aip/journal/pof2/19/4/10.1063/1.2715621>, doi:<http://dx.doi.org/10.1063/1.2715621>.
- 742 [19] Kang, M., Fedkiw, R.P., Liu, X.D., 2000. A boundary condition capturing
 743 method for multiphase incompressible flow. Journal of scientific computing
 744 15, 323–360.
- 745 [20] Khismatullin, D.B., Renardy, Y., Cristini, V., 2003. Inertia-induced
 746 breakup of highly viscous drops subjected to simple shear. Physics of Fluids
 747 15, 1351–1354. doi:<http://dx.doi.org/10.1063/1.1564825>.

- 748 [21] Komrakova, A., Shardt, O., Eskin, D., Derksen, J., 2014. Lattice
 749 boltzmann simulations of drop deformation and breakup in shear flow.
 750 International Journal of Multiphase Flow 59, 24 – 43. URL: <http://www.sciencedirect.com/science/article/pii/S0301932213001547>,
 751 doi:<http://dx.doi.org/10.1016/j.ijmultiphaseflow.2013.10.009>.
- 753 [22] Komrakova, A., Shardt, O., Eskin, D., Derksen, J., 2015. Effects
 754 of dispersed phase viscosity on drop deformation and breakup
 755 in inertial shear flow. Chemical Engineering Science 126, 150 –
 756 159. URL: <http://www.sciencedirect.com/science/article/pii/S000925091400726X>, doi:<http://dx.doi.org/10.1016/j.ces.2014.12.012>.
- 759 [23] Legendre, D., Magnaudet, J., 1998. The lift force on a spherical bubble in
 760 a viscous linear shear flow. Journal of Fluid Mechanics 368, 81–126.
- 761 [24] Li, J., Renardy, Y., Renardy, M., 2000. Numerical simulation of
 762 breakup of a viscous drop in simple shear flow through a volume-of-fluid
 763 method. Physics of Fluids 12, 269–282. URL: <http://scitation.aip.org/content/aip/journal/pof2/12/2/10.1063/1.870305>, doi:<http://dx.doi.org/10.1063/1.870305>.
- 766 [25] Müller-Fischer, N., Tobler, P., Dressler, M., Fischer, P., Windhab, E.J.,
 767 2008. Single bubble deformation and breakup in simple shear flow. Experiments
 768 in fluids 45, 917–926.
- 769 [26] Ohta, M., Akama, Y., Yoshida, Y., Sussman, M., 2014. Influence of the
 770 viscosity ratio on drop dynamics and breakup for a drop rising in an im-
 771 miscible low-viscosity liquid. Journal of Fluid Mechanics 752, 383–409.
 772 doi:[10.1017/jfm.2014.339](https://doi.org/10.1017/jfm.2014.339).
- 773 [27] Ohta, M., Furukawa, T., Yoshida, Y., Sussman, M., 2019. A
 774 three-dimensional numerical study on the dynamics and deformation
 775 of a bubble rising in a hybrid carreau and fene-cr modeled poly-
 776 mERIC liquid. Journal of Non-Newtonian Fluid Mechanics 265, 66–
 777 78. URL: <https://www.sciencedirect.com/science/article/pii/S0377025718301952>, doi:<https://doi.org/10.1016/j.jnnfm.2018.12.012>.
- 780 [28] Ohta, M., Kikuchi, D., Yoshida, Y., Sussman, M., 2011. Robust numeri-
 781 cal analysis of the dynamic bubble formation process in a viscous liquid.
 782 International Journal of Multiphase Flow 37, 1059–1071.
- 783 [29] Ohta, M., Sussman, M., 2012. The buoyancy-driven mo-
 784 tion of a single skirted bubble or drop rising through
 785 a viscous liquid. Physics of Fluids 24, 112101. URL:
 786 <https://doi.org/10.1063/1.4765669>, doi:[10.1063/1.4765669](https://doi.org/10.1063/1.4765669),
 787 arXiv:https://pubs.aip.org/aip/pof/article-pdf/doi/10.1063/1.4765669/14128560/112101_1.pdf

- 788 [30] Rallison, J.M., 1984. The deformation of small viscous drops
 789 and bubbles in shear flows. Annual Review of Fluid Mechanics
 790 16, 45–66. URL: <http://dx.doi.org/10.1146/annurev.fl.16.010184.000401>,
 791 doi:10.1146/annurev.fl.16.010184.000401,
 792 arXiv:<http://dx.doi.org/10.1146/annurev.fl.16.010184.000401>.
- 793 [31] Renardy, Y., 2006. Numerical simulation of a drop undergoing large am-
 794 plitude oscillatory shear. Rheologica acta 45, 223–227.
- 795 [32] Renardy, Y., 2007. The effects of confinement and inertia on the production
 796 of droplets. Rheologica Acta 46, 521–529. URL: <http://dx.doi.org/10.1007/s00397-006-0150-y>,
 797 doi:10.1007/s00397-006-0150-y.
- 798 [33] Renardy, Y., 2008. Effect of startup conditions on drop breakup under
 799 shear with inertia. International Journal of Multiphase Flow
 800 34, 1185 – 1189. URL: <http://www.sciencedirect.com/science/article/pii/S030193220800089X>,
 801 doi:<http://dx.doi.org/10.1016/j.ijmultiphaseflow.2008.04.004>.
- 803 [34] Renardy, Y., Cristini, V., 2001a. Effect of inertia on drop breakup under
 804 shear. Physics of Fluids 13, 7–13. URL: <http://scitation.aip.org/content/aip/journal/pof2/13/1/10.1063/1.1331321>,
 805 doi:<http://dx.doi.org/10.1063/1.1331321>.
- 807 [35] Renardy, Y., Cristini, V., Li, J., 2002. Drop fragment distributions un-
 808 der shear with inertia. International Journal of Multiphase Flow 28, 1125
 809 – 1147. URL: <http://www.sciencedirect.com/science/article/pii/S0301932202000228>,
 810 doi:[http://dx.doi.org/10.1016/S0301-9322\(02\)00022-8](http://dx.doi.org/10.1016/S0301-9322(02)00022-8).
- 812 [36] Renardy, Y.Y., Cristini, V., 2001b. Scalings for fragments produced
 813 from drop breakup in shear flow with inertia. Physics of Fluids 13,
 814 2161–2164. URL: <https://doi.org/10.1063/1.1384469>,
 815 doi:10.1063/1.1384469, arXiv:<https://doi.org/10.1063/1.1384469>.
- 816 [37] Rust, A., Manga, M., 2002. Bubble shapes and orientations in low re
 817 simple shear flow. Journal of Colloid and Interface Science 249, 476–
 818 480. URL: <https://www.sciencedirect.com/science/article/pii/S0021979702982925>,
 819 doi:<https://doi.org/10.1006/jcis.2002.8292>.
- 820 [38] Sharifi, R., Varmazyar, M., Mohammadi, A., 2024. Investigat-
 821 ing droplet and bubble deformation under shear flow us-
 822 ing the multi-pseudo-potential scheme of lattice boltzmann
 823 method. Advances in Applied Mathematics and Mechanics
 824 16, 519–548. URL: <https://global-sci.com/article/72820/investigating-droplet-and-bubble-deformation-under-shear-flow-using-the-multi-pseudo-potential-scheme-of-lattice-boltzmann-method>,
 825 doi:<https://doi.org/10.4208/aamm.OA-2021-0326>.

- 827 [39] Stone, H.A., 1994. Dynamics of drop deformation and breakup
 828 in viscous fluids. Annual Review of Fluid Mechanics 26,
 829 65–102. URL: <http://dx.doi.org/10.1146/annurev.fl.26.010194.000433>,
 830 doi:10.1146/annurev.fl.26.010194.000433, arXiv:<http://dx.doi.org/10.1146/annurev.fl.26.010194.000433>.
- 832 [40] Sussman, M., 2003. A second order coupled level set and volume-
 833 of-fluid method for computing growth and collapse of vapor bubbles.
 834 Journal of Computational Physics 187, 110–136. URL: <https://www.sciencedirect.com/science/article/pii/S0021999103000871>,
 835 doi:[https://doi.org/10.1016/S0021-9991\(03\)00087-1](https://doi.org/10.1016/S0021-9991(03)00087-1).
- 837 [41] Sussman, M., Almgren, A.S., Bell, J.B., Colella, P., Howell, L.H.,
 838 Welcome, M.L., 1999. An adaptive level set approach for incom-
 839 pressible two-phase flows. Journal of Computational Physics 148, 81
 840 – 124. URL: <http://www.sciencedirect.com/science/article/pii/S002199919896106X>, doi:<https://doi.org/10.1006/jcph.1998.6106>.
- 842 [42] Sussman, M., Puckett, E.G., 2000. A coupled level set and
 843 volume-of-fluid method for computing 3d and axisymmetric incompress-
 844 ible two-phase flows. Journal of Computational Physics 162, 301–
 845 337. URL: <http://www.sciencedirect.com/science/article/pii/S0021999100965379>, doi:<http://dx.doi.org/10.1006/jcph.2000.6537>.
- 847 [43] Sussman, M., Smereka, P., Osher, S., 1994. A level set ap-
 848 proach for computing solutions to incompressible two-phase flow.
 849 Journal of Computational Physics 114, 146 – 159. URL: <http://www.sciencedirect.com/science/article/pii/S0021999184711557>,
 850 doi:<http://dx.doi.org/10.1006/jcph.1994.1155>.
- 852 [44] Sussman, M., Smith, K., Hussaini, M., Ohta, M., Zhi-Wei, R., 2007. A
 853 sharp interface method for incompressible two-phase flows. Journal of Com-
 854 putational Physics 221, 469–505. URL: <https://www.sciencedirect.com/science/article/pii/S0021999106002981>, doi:<https://doi.org/10.1016/j.jcp.2006.06.020>.
- 857 [45] Tanguy, S., Ménard, T., Berlemont, A., 2007. A level set method for
 858 vaporizing two-phase flows. Journal of Computational Physics 221, 837–
 859 853.
- 860 [46] Tatebe, O., 1993. The multigrid preconditioned conjugate gradient method,
 861 in: NASA. Langley Research Center, The Sixth Copper Mountain Confer-
 862 ence on Multigrid Methods, Part 2.
- 863 [47] Taylor, G.I., 1932. The viscosity of a fluid containing small drops of another
 864 fluid. Proceedings of the Royal Society of London A: Mathematical, Phys-
 865 ical and Engineering Sciences 138, 41–48. doi:10.1098/rspa.1932.0169.

- 866 [48] Taylor, G.I., 1934. The formation of emulsions in definable fields of flow.
 867 Proceedings of the Royal Society of London A: Mathematical, Physical and
 868 Engineering Sciences 146, 501–523. doi:10.1098/rspa.1934.0169.
- 869 [49] Unverdi, S.O., Tryggvason, G., 1992. A front-tracking method
 870 for viscous, incompressible, multi-fluid flows. Journal of Computational
 871 Physics 100, 25 – 37. URL: <http://www.sciencedirect.com/science/article/pii/002199919290307K>, doi:[http://dx.doi.org/10.1016/0021-9991\(92\)90307-K](http://dx.doi.org/10.1016/0021-9991(92)90307-K).
- 874 [50] Wang, A., Evans, G., Mitra, S., 2023. A review of bubble
 875 surface loading and its effect on bubble dynamics. Minerals
 876 Engineering 199, 108105. URL: <https://www.sciencedirect.com/science/article/pii/S089268752300119X>, doi:<https://doi.org/10.1016/j.mineng.2023.108105>.
- 879 [51] Wang, Z., Shi, D., Zhang, A., 2015. Three-dimensional lattice boltzmann
 880 simulation of bubble behavior in a flap-induced shear flow. Computers & Fluids 123, 44 – 53. URL: <http://www.sciencedirect.com/science/article/pii/S0045793015003199>, doi:<https://doi.org/10.1016/j.compfluid.2015.09.007>.
- 884 [52] Wei, Y.K., Qian, Y., Xu, H., 2012. Lattice boltzmann simulations
 885 of single bubble deformation and breakup in a shear flow. The Journal
 886 of Computational Multiphase Flows 4, 111–117. URL: <https://doi.org/10.1260/1757-482X.4.1.111>, doi:10.1260/1757-482X.4.1.111, arXiv:<https://doi.org/10.1260/1757-482X.4.1.111>.
- 889 [53] Yoshikawa, H.N., Zoueshtiagh, F., Caps, H., Kurowski, P., Petitjeans, P.,
 890 2010. Bubble splitting in oscillatory flows on ground and in reduced gravity.
 891 The European Physical Journal E 31, 191–199.
- 892 [54] Zhang, J., Miksis, M.J., Bankoff, S.G., 2006. Nonlinear dynamics of
 893 a two-dimensional viscous drop under shear flow. Physics of Fluids
 894 18. URL: <http://scitation.aip.org/content/aip/journal/pof2/18/7/10.1063/1.2222336>, doi:<http://dx.doi.org/10.1063/1.2222336>.
- 896 [55] Zhang, J., Ni, M.J., Magnaudet, J., 2021a. Three-dimensional dynamics
 897 of a pair of deformable bubbles rising initially in line. part 1. moderately
 898 inertial regimes. Journal of Fluid Mechanics 920, A16.
- 899 [56] Zhang, J., Ni, M.J., Magnaudet, J., 2022. Three-dimensional dynamics of
 900 a pair of deformable bubbles rising initially in line. part 2. highly inertial
 901 regimes. Journal of Fluid Mechanics 943, A10.
- 902 [57] Zhang, J., Shu, S., Guan, X., Yang, N., 2021b. Regime mapping
 903 of multiple breakup of droplets in shear flow by phase-field
 904 lattice boltzmann simulation. Chemical Engineering Science 240,
 905 116673. URL: <https://www.sciencedirect.com/science/article/>

906 pii/S0009250921002384, doi:<https://doi.org/10.1016/j.ces.2021.116673>.

908 [58] Zhang, W., Almgren, A., Beckner, V., Bell, J., Blaschke, J., Chan, C.,
909 Day, M., Friesen, B., Gott, K., Graves, D., Katz, M., Myers, A., Nguyen,
910 T., Nonaka, A., Rosso, M., Williams, S., Zingale, M., 2019. AMReX: a
911 framework for block-structured adaptive mesh refinement. Journal of Open
912 Source Software 4, 1370. URL: <https://doi.org/10.21105/joss.01370>,
913 doi:10.21105/joss.01370.